

● *Original Contribution*

ULTRASOUND-INDUCED BUBBLE CLUSTERS IN TISSUE-MIMICKING AGAR PHANTOMS

POOYA MOVAHED,* WAYNE KREIDER,[†] ADAM D. MAXWELL,^{†‡} BARBRINA DUNMIRE,[†]
and JONATHAN B. FREUND*[§]

*Department of Mechanical Science and Engineering, University of Illinois at Urbana–Champaign, Urbana, IL, USA; [†]Center for Industrial and Medical Ultrasound, Applied Physics Laboratory, University of Washington, Seattle, WA, USA; [‡]Department of Urology, University of Washington School of Medicine, Seattle, WA, USA; and [§]Department of Aerospace Engineering, University of Illinois at Urbana–Champaign, Urbana, IL, USA

(Received 15 February 2017; revised 17 May 2017; in final form 15 June 2017)

Abstract—Therapeutic ultrasound can drive bubble activity that damages soft tissues. To study the potential mechanisms of such injury, transparent agar tissue-mimicking phantoms were subjected to multiple pressure wave bursts of the kind being considered specifically for burst wave lithotripsy. A high-speed camera recorded bubble activity during each pulse. Various agar concentrations were used to alter the phantom's mechanical properties, especially its stiffness, which was varied by a factor of 3.5. However, the maximum observed bubble radius was insensitive to stiffness. During 1000 wave bursts of a candidate burst wave lithotripsy treatment, bubbles appeared continuously in a region that expanded slowly, primarily toward the transducer. Denser bubble clouds are formed at higher pulse repetition frequency. The specific observations are used to inform the incorporation of damage mechanisms into cavitation models for soft materials. (E-mail: pooyam@illinois.edu) © 2017 World Federation for Ultrasound in Medicine & Biology.

Key Words: Cavitation, Bubble dynamics, Bubble cluster, Viscoelastic medium, Agar phantom, Burst wave lithotripsy, Tissue injury.

INTRODUCTION

Acoustic cavitation is common in biomedical applications of ultrasound. It can be used for mechanical fractionation in histotripsy, which produces and maintains a dense bubble cloud for controlled tissue liquefaction. In typical cases, it is driven by short ($<50 \mu\text{s}$) ultrasound pulses at low duty cycles ($<1\%$), with peak positive pressure of up to ~ 100 MPa and peak negative pressure of up to ~ 20 MPa (Roberts et al. 2006; Vlasisavljevich et al. 2014; Wang et al. 2012). Tissue ablation is achieved by fractionation into a liquefied acellular homogenate (Hall et al. 2007; Hempel et al. 2011; Xu et al. 2004). High-intensity pressure waves are also delivered in shock-wave lithotripsy (SWL), currently the most common treatment for kidney stone comminution. It also is a multiple-pulse process; typical treatments entail more than 1000 compressive ≥ 20 MPa shocks followed by weaker (up to ~ 10 MPa) rarefactions (Bailey et al.,

2005; Evan et al., 1998, 2002). The particular therapy that motivates the present effort is a novel technology presented as a potential alternative to SWL called *burst wave lithotripsy* (BWL). Instead of shocks, it uses high-intensity bursts of focused ultrasound to fragment kidney stones. The control available in BWL, particularly wave frequency and pressure amplitude, is hoped to provide flexibility in tailoring the incident pulse for safer and quicker treatments. In some cases, BWL has been shown capable of breaking natural and artificial stones at pressure levels that do not cause injury (Maxwell et al. 2015). However, treatment with high-intensity focused ultrasound (HIFU) naturally risks collateral damage to tissue. A goal is to design general BWL techniques and procedures that avoid such injury, which may occur similarly to what has been reported for SWL (Bailey et al. 2005; Evan et al. 1998, 2002). An understanding of the mechanisms and thresholds will guide this goal and maintain safety. For BWL, we seek to document and understand the mechanisms of bubble activity in tissue-like materials.

To pursue this objective, we designed the experiment shown in Figure 1 for a series of investigations of

Address correspondence to: Pooya Movahed, 1206 West Green Street, Urbana, IL 61801, USA. E-mail: pooyam@illinois.edu

bubble dynamics induced by BWL bursts in gel phantoms. To facilitate observations, transparent agar hydrogels are used (Daniels *et al.* 1987). Gel stiffness is dependent on the agar concentration, which is adjusted. We note, in doing this, that the BWL pulse used in this work has a higher intensity than is expected to be necessary for kidney stone comminution to facilitate the formation and observations of bubble clusters in agar phantoms. These particular measurements are designed to inform the development of cavitation-induced damage models in soft materials, specifically a Rayleigh–Plesset-like bubble dynamics and damage model (Movahed *et al.* 2016).

While our focus is on cavitation in tissue-mimicking soft materials for their transparency, ultrasound-induced cavitation has also been reported in both *ex vivo* and *in vivo* tissues. Vlasisavljevich *et al.* (2015) studied the role of ultrasound frequency and tissue stiffness on the intrinsic threshold for histotripsy-driven cavitation. Passive cavitation detection was used for a histotripsy pulse with 1–2 cycles and frequencies in the range between 345 kHz and 3 MHz, and it was concluded that the possibility of bubble cloud formation is insignificantly affected by tissue stiffness or ultrasound frequency. In another study, an HIFU-guided therapy was developed for non-invasive tissue ablation in a pig model (Khokhlova *et al.* 2014). It was shown that HIFU-induced bubbles are capable of destroying the target tissue by mechanical disruption (rather than by thermal heating).

The experimental setup, measured BWL waveforms, and agar phantom preparation and mechanical properties are described in the next section. We then present the main experimental observations of bubble clusters in agar phantoms with various stiffnesses,

such as shown in Figure 2. Various statistics of the geometry of identified bubbles, such as radius, orientation and aspect ratio, are quantified. Most bubbles appear to remain nearly circular in the imaged plane, and a Rayleigh–Plesset-type bubble dynamics model with damage (Movahed *et al.* 2016) is applied to explain the experimental observations. The bubble cluster tends to move toward the transducer as it develops after consecutive bursts. This behavior is also observed in thermal HIFU (Khokhlova *et al.* 2006; Meaney *et al.* 2000; Watkin *et al.* 1996) and is quantified here by tracking the centroid of all bubbles. We summarize the main conclusions in the final section of this report.

MATERIALS AND METHODS

BWL system

A schematic of the experiment is shown in Figure 1. A piezoelectric ultrasound transducer driven by a DE1 field-programmable gate array logic board (Altera, San Jose, CA, USA) with frequency of 335 kHz generates the focused BWL pulses. The transducer has an array of 6 focused elements, each with a 38-mm diameter and a 120-mm radius of curvature. The overall aperture of the transducer array was 110 mm × 104 mm. The effective beam axial and lateral width are 58 mm and 6 mm, respectively. This nominal focus region was the center of the agar target, which was suspended in a degassed water bath. Pulse repetition frequencies (PRF) were 40, 100 and 200 Hz.

A 20,000 frames-per-second camera (APX-RS, Photron USA, Inc., San Diego, CA, USA) with a Nikkor-P lens (Nikon, Tokyo, Japan) and a continuous backlight source were used to record shadowgraphic

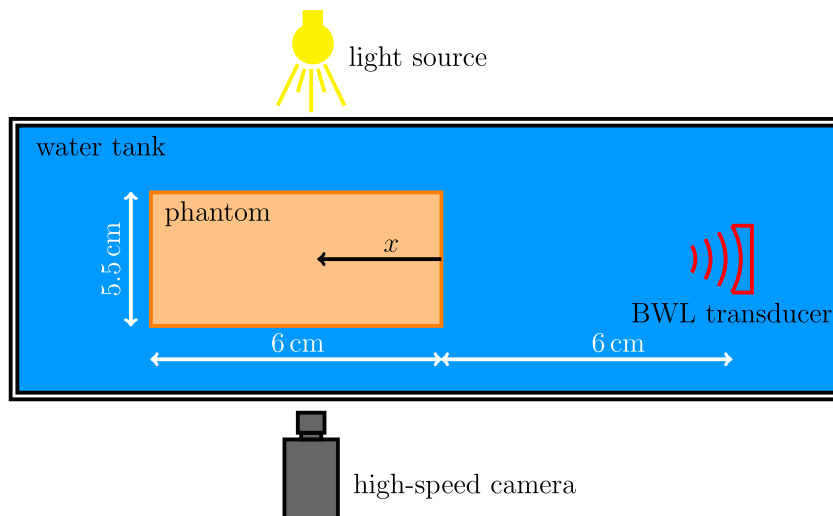


Fig. 1. Schematic of the experimental setup (*not to scale*).

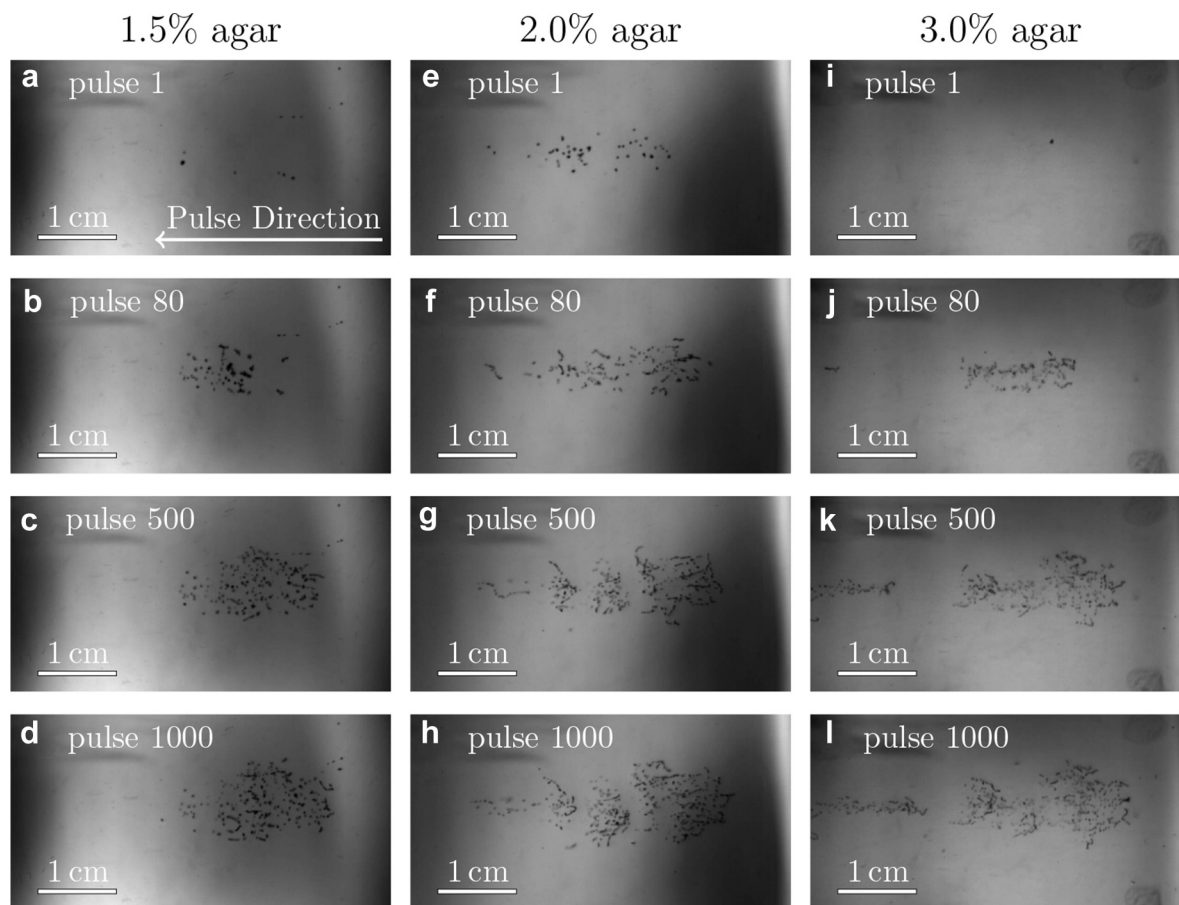


Fig. 2. Bubbles in agar gels with properties as labeled. The region shown is $4.42 \text{ cm} \times 2.27 \text{ cm}$. The BWL pulse has 20 nominal cycles with base frequency 335 kHz, peak negative amplitude of 7.51 MPa and repeats at 200 Hz. Images are shown at 10 cycles into the pulse (*number as labeled*).

images of bubble activity. The camera was triggered to record 1 image for each BWL pulse applied at 10 cycles into that particular pulse. The exposure time was $4 \mu\text{s}$ for all images. As set up, the camera pixel resolution is $58 \mu\text{m}$.

Focal pressure

An FOPH2000 fiberoptic hydrophone (RP Acoustics, Leutenbach, Germany) in a degassed water bath was used to measure the focal pressures shown in Figure 3. The pulse is well-fitted by

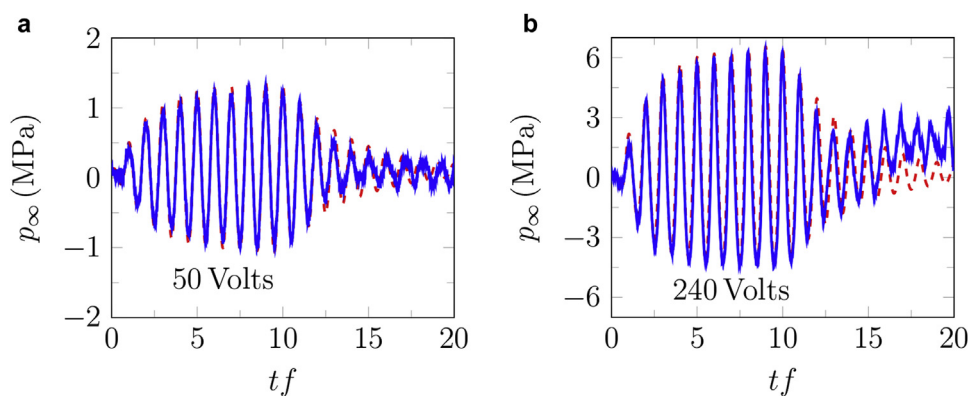


Fig. 3. Incident BWL pulse with $n = 10$ cycles, and $f = 335 \text{ kHz}$; modeled based on (1) (*red*) and measured experimentally (*blue*).

$$p_{\infty}(t) = p_{\text{amb}} + p_{\text{max}}^{-} \gamma(t) \cos(2\pi ft) \times \left[\left(1 - \exp\left[-\frac{t}{\tau_1}\right] \right) \frac{1 + \tanh\left(\frac{t}{\tau_2}\right)}{2} - \left(1 - \exp\left[\frac{t-n}{\tau_2}\right] \right) \frac{1 + \tanh(tf-n)}{2} \right], \quad (1)$$

where

$$\gamma(t) = 1 + \frac{p_{\text{max}}^{+}/p_{\text{max}}^{-} - 1}{2} [1 + \cos(2\pi ft)], \quad (2)$$

accounts for the asymmetric peak amplitude. In these measurements, the ambient pressure is $p_{\text{amb}} = 0.1$ MPa, p_{max}^{-} is the peak negative amplitude, p_{max}^{+} is the peak positive amplitude, $f = 335$ kHz is the frequency, $n = 10$ is the nominal number of cycles, and $\tau_1 = 5 \mu\text{s}$ and $\tau_2 = 12 \mu\text{s}$ are the rise and fall times for the pulse envelop.

The rough appearance of the trace at the end of the pulse for 240 V (Fig. 3b) is an artifact of cavitation on the hydrophone (Maxwell *et al.* 2013), which unfortunately precludes accurate measurement of higher-amplitude waveforms. Thus, measurements were taken up to a transducer voltage of 240 V. The peak positive and negative pressures increase approximately linearly with the transducer voltage (Fig. 4a), with the peak positive pressure about 35% higher than the corresponding negative pressure for ≥ 200 V, as shown in Figure 4b. A linear fit to the data suggests

$$\begin{cases} p_{\text{max}}^{-} = 19.0 \text{ (kPa/Volt)} V + 220 \text{ (kPa)} \\ p_{\text{max}}^{+} = 26.7 \text{ (kPa/Volt)} V - 50 \text{ (kPa)} \end{cases}, \quad (3)$$

where V is the applied voltage on the transducer. Based on (3), p_{max}^{-} and p_{max}^{+} are estimated to be 7.51 and 10.09 MPa for 383.3 V. The pressure amplitude is approximately constant for more than 10 cycles. Except where noted, pulses had 20 cycles with base frequency 335 kHz, peak negative amplitude of 7.51 MPa and repeated at 200 Hz. The hydro-

phone was more prone to cavitation for more cycles, which is why only 10 cycles were used here. As is clear in Figure 3, this was sufficient for measuring the ring-up and ring-down periods as well as the quasi-steady signal in between.

Agar phantoms

Agar hydrogels are commonly used as phantoms to mimic tissue (Daniels *et al.* 1987; Dunnire *et al.* 2013; Vlaisavljevich *et al.* 2014). We prepared our hydrogels with agar concentrations 1.5%–3.0% w/v and with a water:dimethyl sulfoxide (DMSO, 99% purity, FWI, Tulsa, OK, USA) ratio of 30:20 to improve optical clarity following established protocols (Dunnire *et al.* 2013; Hall *et al.* 1997; Hyon *et al.* 1989). To minimize gas content, the agar, DMSO and water were mixed and heated to boiling on a magnetic stir plate. The solution was then cooled to 70°C, whereupon it was poured into a plastic 5.5 cm \times 5.5 cm \times 6 cm mold. The solution was covered and allowed to cool to room temperature and solidify. After solidification, the phantom was rinsed with water for a day so that the DMSO is replaced with water to minimize optical diffraction by DMSO gradient within the gel phantom.

The elastic resistance of agar phantoms increases with increasing agar concentration (Normand *et al.*, 2000). We measured the small-strain Young's modulus Y for various agar concentrations with micro-indentometry (Choi and Shield 1981) to be 105, 175 and 347 kPa for 1.5%, 2.0% and 3.0% agar phantoms, respectively.

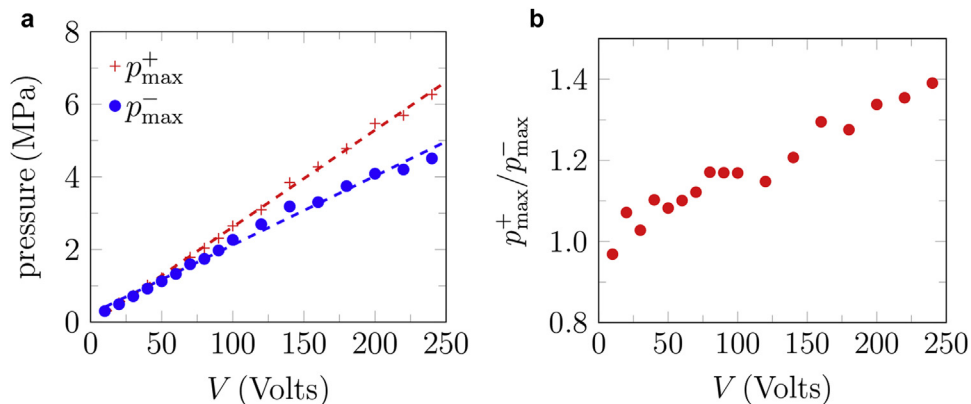


Fig. 4. Pressure measurements at the focal point: (a) peak positive and negative pressure, and (b) the ratio of the peak positive to the negative pressure.

RESULTS

Each agar phantom was exposed to 1000 bursts of the kind shown in Figure 3, although with 20 cycles. This was repeated $10\times$ for each agar concentration at the same site. During the initial pulses, only isolated bubbles are observed, as seen in Figure 2. It is thought that these first bubbles arise from bubble nuclei with initial radius of $\lesssim 1\ \mu\text{m}$, which are distributed within each gel but not resolved with these measurements. The tensile portions of the delivered bursts cause these to expand sufficiently to become visible. The bubble dynamics are quick, so we must be cognizant of the framing rate and exposure time in making our assessments of bubble dynamics based upon the images. The camera frame rate was set to match the PRF so there is 1 image per pulse. The exposure time was $4\ \mu\text{s}$, and images were recorded at the pulse midpoint, 10 cycles into the pulse. This is the shortest exposure time that provides sufficient backlight. On the basis of the Rayleigh–Plesset model, the bubble period is expected to match the $2.98\ \mu\text{s}$ period of the BWL pulse (Movahed et al. 2016), so the exposure time of $4\ \mu\text{s}$ is expected to be long enough to capture the bubble throughout a full cycle of oscillation. Hence, even though the backlit images are expected to exhibit some motion-induced blur, the extent of the observed shadow provides an estimate of the maximum bubble radius. It was noted that the bubble clouds, such as in Figure 2, might appear to have a structure, but no specific and repeatable patterns were quantified.

Bubble identification and statistics

To quantify bubbles, a background image is first subtracted from the raw gray-scale images, such as in Figure 2, to remove the backlight non-uniformity. Then, linear interpolation is used to obtain the intensity on a $4\times$ finer grid. This makes subsequent identification of angles less sensitive to the pixel size of the images. Finally, images were converted to binary black and white on the basis of an intensity threshold following Otsu's well-established method (Otsu 1975) as implemented in the graythresh function in image-processing software (MATLAB, MathWorks, Natick, MA, USA).

The total viewed area of all identified bubbles is designated ϕ and plotted in Figure 5, which quantifies the bubble coverage as more pulses are delivered to the same site (Fig. 2). A fatigue-based model for this was developed and reported elsewhere (Movahed et al. 2016). This work suggests that material fatigue and eventual irreversible fracture-like failure is responsible for the observed behavior. Herein we focus on new observations regarding the evolution of the bubbles undergoing inertial

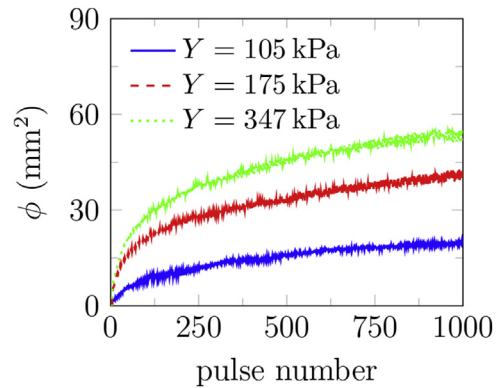


Fig. 5. The total area of all identified bubbles ϕ versus pulse number. Each curve is an average over 10 trials for each gel stiffness.

cavitation. Because bubble activity is widespread and persistent, it is expected to be generally important for tissue injury.

To quantify the geometry and orientation of bubbles, an ellipse is fitted to each identified bubble in the black-and-white images as implemented in the regionprops routine of MATLAB (MathWorks) (Fig. 6) (Hamaguchi and Ando 2015). The fitted ellipse has the same normalized second central moments as the white region in black-and-white images (Haralock and Shapiro 1992). Then, a radius-like bubble length scale is defined

$$R = \sqrt{\frac{\text{Area}}{\pi}}. \quad (4)$$

The ratio of major to minor axes β of the fitted ellipse shown in Figure 6 measures the bubble circularity. Consequently, we report data for $\beta < 1.05$ and 1.1 to restrict the statistics only to nearly circular features based on their 2-D projection images. Examples of the identified bubbles for various thresholds are shown in Figure 7.

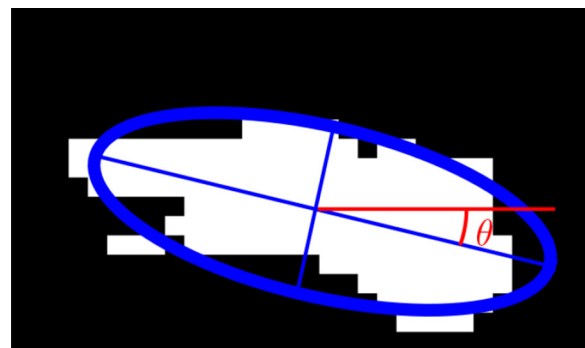


Fig. 6. An example of a fitted ellipse to an area with bubble activity in the image processing software. θ represents the angle between the major axis of the fitted ellipse and a horizontal line parallel to the transducer axis.

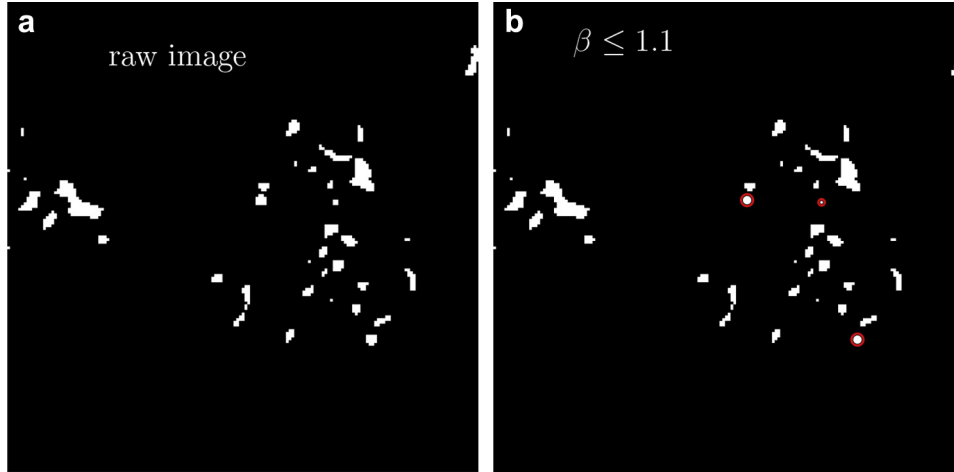


Fig. 7. Examples of bubble identification for $\beta \leq 1.1$ in the image processing software. Identified circular bubbles are indicated by a *red circle*.

The maximum bubble radius R_{\max} is calculated for each of the $N = 10^4$ images, and the average maximum bubble radius \bar{R}_{\max} and its standard deviation are defined as

$$\bar{R}_{\max} = \frac{1}{N} \sum_{i=1}^N R_{\max,i}, \quad SD_{R_{\max}} = \sqrt{\sum_{i=1}^N \frac{1}{N} (R_{\max,i} - \bar{R}_{\max})^2}. \quad (5)$$

These are reported in [Figure 8](#) for various agar concentrations, which shows stiffness insensitivity. It also confirms that these results are insensitive to the threshold for values of β , although increasing this threshold also increases \bar{R}_{\max} because less circular features are also included in the average in this case. However, the conclusion is insensitive to this: \bar{R}_{\max} is insensitive to elastic resistance for the considered range ($105 \text{ kPa} \leq Y \leq$

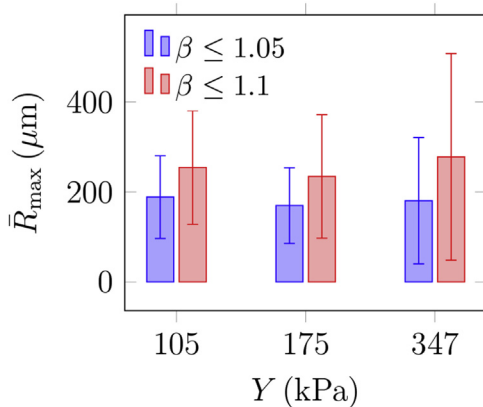


Fig. 8. The average maximum bubble radius \bar{R}_{\max} and its standard deviation (error bars) from (5) for different values of Young's modulus.

347 kPa). Insensitivity of \bar{R}_{\max} to stiffness and observations of more bubbles for stiffer gels ([Fig. 5](#)) imply that the bubble number density increases with agar concentration. This suggests that a higher agar concentration leads to more nucleation sites.

Additional geometric information can be quantified on the basis of the fitted ellipses: the inclination angle θ relative to the burst propagation ([Fig. 6](#)), the asymmetry *via* the ratio of the major to minor axis β and of course the perimeter L and area A . The probability density function (PDF) of all features is shown in [Figure 9](#). The PDF determines the possibility of a random variable V falling within a specific range. The PDF is always positive and satisfies

$$\int_{-\infty}^{\infty} \text{PDF}(V) dV = 1. \quad (6)$$

PDF(θ) shows that these features are distributed at various. The most observed orientation is parallel to the transducer axis. Because $\beta = 1$ for a circle, the β distribution shows that, indeed, most features are nearly circular, with probabilities of larger β decreasing rapidly. Features with β longer than 4 are essentially not observed. For nearly circular features, Rayleigh–Plesset-type bubble dynamics models are expected to be a good representative of the overall dynamics of observed bubbles and will be discussed in the *Isolated single-bubble dynamics simulations* section of this report. Although the maximum observed bubble sizes are insensitive to the gel stiffness, the most probable bubble sizes show a clear trend. The most expected value for bubble radius, $\langle R \rangle$, based on the probability distributions for either area or perimeter (as illustrated in [Fig. 10](#)) shows that it decreases with Y . Physical interpretation of R_{\max} and $\langle R \rangle$ and their dependence on Y is discussed in the next section.

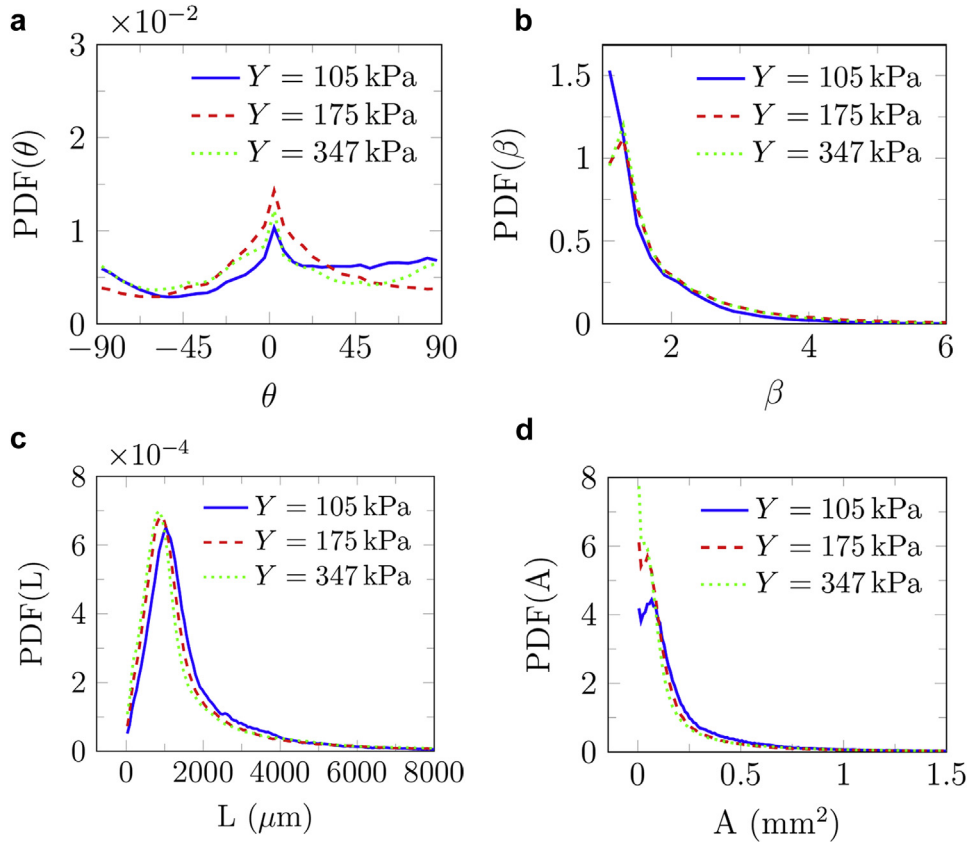


Fig. 9. Probability density function of (a) angle θ (see Fig. 6), (b) major to minor axis ratio β , (c) perimeter L and (d) area A of features observed for different gel stiffnesses.

Isolated single-bubble dynamics simulations

The Rayleigh–Plesset equation (Plesset and Prosperetti 1977; Rayleigh 1917) describes the dynamics of a bubble with finite surface tension in a viscous, incompressible, Newtonian fluid subjected to far-field pressure variation. Here, the basic formulation has been augmented to include the effect of finite-

deformation elasticity on bubble dynamics in viscoelastic soft materials. The elastic response of the infinite surrounding medium has already been extended to linear elastic, neo-Hookean and Fung models (Movahed et al. 2016; Yang and Church 2005). These models quantify confinement mechanisms of bubbles within soft materials. Furthermore, the material close to the bubble surface can be highly strained, with the consequence of potential irreversible damage that degrades elastic and viscous characteristics. The onset of damage is determined from the fracture theory.

We further augment a Rayleigh–Plesset-like bubble dynamics model with fracture-like damage mechanisms (Movahed et al. 2016) to describe the simultaneous elastic insensitivity of \bar{R}_{max} and sensitivity of $\langle R \rangle$. In this description, the bubble dynamics is governed by (Movahed et al. 2016)

$$\left(1 - \frac{\dot{R}}{c}\right)R\ddot{R} + \frac{3}{2}\left(1 - \frac{\dot{R}}{3c}\right)\dot{R}^2 = \frac{1}{\rho}\left(1 + \frac{\dot{R}}{c}\right)Q + \frac{R}{\rho c} \frac{d}{dt}Q, \tag{7}$$

where R is the bubble radius, \dot{R} and \ddot{R} are velocity and acceleration at the bubble surface, $c = 1480 \text{ ms}^{-1}$ and $\rho =$

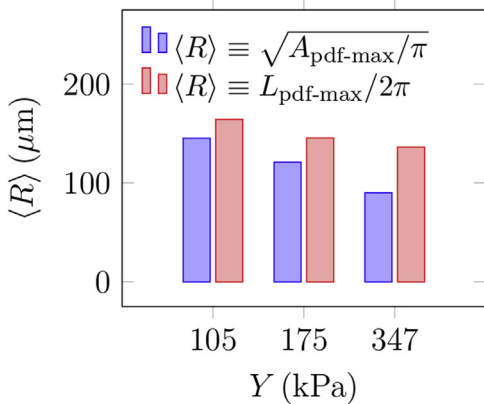


Fig. 10. The most expected bubble radius for various agar gel stiffnesses.

1012.8 kgm^{-3} are the sound speed and the density of the surrounding medium, respectively, and

$$Q = p_B - p_\infty - \frac{2S}{R} - (1-\alpha) \left(\frac{4\mu\dot{R}}{R} - E \right), \quad (8)$$

where p_B is the internal bubble pressure modeled as a polytropic gas, $p_\infty(t)$ is the pressure of the passing BWL pressure pulse, $S = 0.073 \text{ N/m}$ is the surface tension, μ is the viscosity and E represents the confinement effects of elasticity (Movahed *et al.*, 2016). The viscoelastic behavior of the gel is represented by a non-linear Kelvin–Voigt model, and its strain hardening is represented by the Fung model. Under cyclic large deformation, stress softening is expected (Martins dos Santos *et al.* 1997) and is represented by the factor α . The full details of the model are presented elsewhere (Movahed *et al.* 2016).

Viscosity measurements that meet our conditions, which involve high strain and high-strain rate, are not yet available. However, sufficient data support that agar gels are highly viscous. Here, we report results for $\mu = 1.0 \text{ Pa s}$, and various values of the fatigue factor α , although our conclusions do not hinge on these specific values. The simulated maximum bubble radius with initial radius of $0.1 \text{ }\mu\text{m}$ exposed to a BWL pulse with 10 cycles is shown in Figure 11 for α between 0 and 1, which corresponds to intact and fully damaged conditions, respectively. The BWL pulse is approximated using (1), and a pulse with 10 cycles are considered because camera images were recorded after 10 cycles. With this interpretation, for our experiments the maximum observed bubble radius occurs at highly damaged sites in which the maximum bubble radius becomes insensitive to the gel's stiffness, in agreement with our experiments. On the other hand, the expectation radius $\langle R \rangle$ is based on the distribution and includes cavitation sites with a lower extent of damage in which the maximum bubble radius

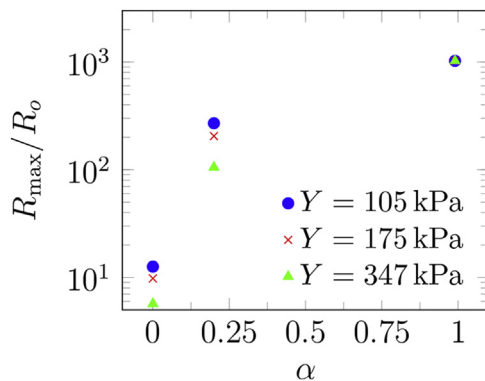


Fig. 11. Simulated maximum bubble radius versus fatigue factor α for different agar gel stiffness.

remains sensitive to the gel's stiffness. Thus, as observed, $\langle R \rangle$ should depend on the gel's stiffness.

Cloud evolution

Images such as in Figure 2 suggest that regions with bubble activity migrate toward the transducer. To quantify this, we define a nominal centroid of all bubbles

$$C_x = \frac{1}{N} \sum_{i=1}^N x_i A_i, \quad (9)$$

where N is the number of observed bubbles, and x_i and A_i are the centroid and area of each (Fig. 12a). Although we found fluctuations in C_x because of the apparently stochastic character of the bubbles, Figure 12b shows that C_x consistently decreases similar to that reported in thermal HIFU (Khokhlova *et al.* 2006; Meaney *et al.* 2000; Watkin *et al.* 1996).

Because thermal heating is thought to dominate material degradation in HIFU, lesion evolution of this kind was described by a so-called bioheat (Pennes 1948) equation, which includes thermal conduction, attenuation-based models for ultrasound energy deposition (Kolios *et al.* 1996; Robinson and Lele 1972), both convective and perfusion-driven cooling and thermal capacity of the tissue (Coussios and Roy 2008). Numerical solutions (Meaney *et al.* 2000) suggest that the lesion should evolve toward the transducer and that non-linear wave propagation contributes to this phenomenon. However, the present observation introduces a curious question. With a duty cycle of 1.2%, the estimated mean energy deposition rate excluding bubble-enhanced heating (Coussios and Roy 2008) is

$$I = \gamma \frac{p_{\text{rms}}^2}{\rho c} = 2.36 \text{ kW/cm}^2, \quad (10)$$

where $\gamma = 0.9 \text{ m}^{-1}$ is the attenuation coefficient for agar gel (Zell *et al.* 2007) and $p_{\text{rms}} = 6.28 \text{ MPa}$ is the root mean square of the BWL pressure pulse. This would elevate the temperature in the focus by only 0.36°C for 1000 pulses. This increase is small, and the actual rise is anticipated to be smaller because it neglects any cooling. This, in turn, suggests a mechanism for the observed migration that does not involve substantive mean heating. This could be purely mechanical or might involve relatively transient thermal phenomena (Bailey *et al.* 2001).

Simulation of HIFU suggests that scattering from bubbles in the focal region affects the spreading phenomenology (Chavrier *et al.* 2000). In these treatments, cavitation may lead to pre-focal heating, movement of lesions toward the transducer and inhomogeneous HIFU-induced lesions in the target area, which is

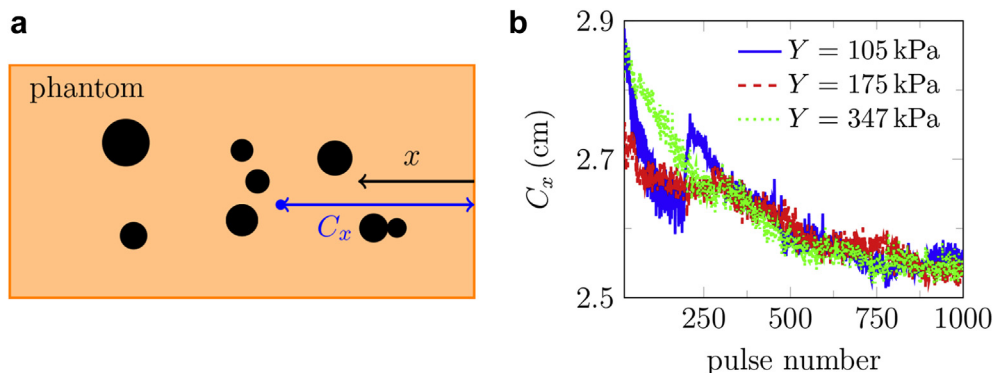


Fig. 12. (a) Schematic of the centroid of all bubbles C_x within the gel, (b) the centroid of all bubbles C_x versus pulse number for various agar concentrations. Bubbles tend to move toward the transducer. The reported data are the average of 10 trials in each gel.

undesirable (Chavrier et al. 2000; Sanghvi et al. 1996). We expect that, similar to thermal HIFU (Chavrier et al. 2000), wave scattering from the bubbles initially excited in agar phantoms increases the pressure pre-focally, allowing those bubbles to expand sufficiently to become visible on images, which results in the movement of the centroid of all bubbles toward the transducer as shown in Figure 12.

Role of PRF

Previous studies of SWL suggest that reducing the PRF results in better stone fragmentation and, consequently, improves the stone passage rate (Paterson et al. 2002; Pishchalnikov et al. 2003, 2006; Rassweiler et al. 2011). However, reducing the PRF prolongs treatment time and cost and patient inconvenience. In general, more cavitation is expected at higher PRF, and rectified diffusion is proposed as a possible mechanism (Crum 1982; Sapozhnikov et al. 2002). To study the role of PRF on bubble-cloud evolution in the context of BWL,

we repeated our experiments at PRF = 40, 100 and 200 Hz. The rate of bubble-cloud formation is tracked by plotting the total area of all bubbles in Figure 13a. Results for various numbers of cycles at PRF = 200 Hz are reported in Figure 13b. More bubbles appear continuously for all cases, and ϕ at the last pulse increases monotonically with PRF and numbers of cycles. This is in agreement with the common expectation that the extent of the cavitation and the subsequent induced damage can be suppressed at lower PRF and fewer cycles per burst for BWL. A better understanding of the role of ultrasound parameters on stone comminution is still needed to optimize this technology. On the basis of our current investigations, we expect that safe and fast treatment is plausible for PRF between 40 and 200 Hz.

CONCLUSIONS

An experimental setup is developed to investigate cavitation in agar tissue-mimicking phantoms. Gel

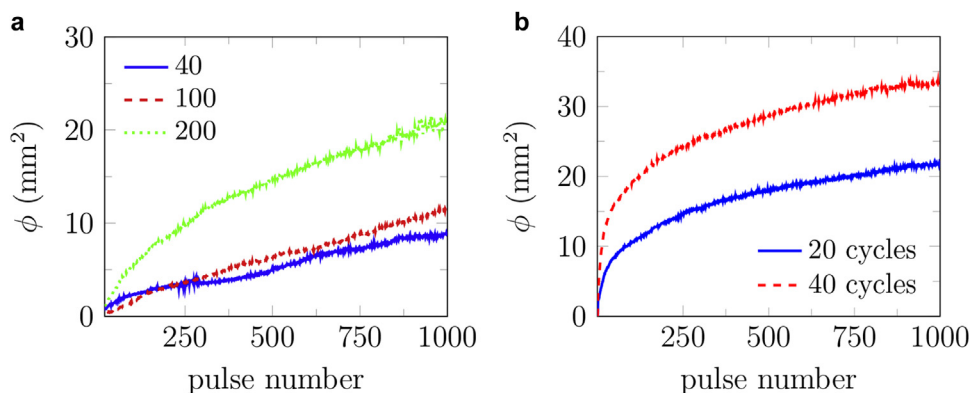


Fig. 13. The total area of all identified bubbles ϕ versus pulse number for 2% agar at (a) 20 cycles and various pulse repetition frequencies, and (b) PRF = 200 and various numbers of cycles. Images were recorded at 10 and 30 cycles into the pulse number for 20- and 40-cycle bursts, respectively. The reported results are the average of 10 trials in each gel. PRF = pulse repetition frequencies.

stiffness is adjusted by varying agar concentration. Bubble observations are reported to inform a class of damage models (Movahed *et al.* 2016) and motivate the development of cavitation-induced damage models. Images of bubbles in transparent tissue-mimicking agar phantoms from a high-speed camera subjected to BWL pulses showed inertial cavitation at multiple sites during the initial pulses, with the further continuous appearance of large bubbles at new locations throughout the course of the observations. The lag in the onset of cavitation is explained by a Rayleigh–Plesset-type bubble dynamics model with a damage mechanism based on fracture and fatigue (Movahed *et al.* 2016).

The statistics on the bubble geometry show that most bubbles remain nearly circular. The overall bubble cloud expands and tends to move toward the transducer during consecutive pulses. This is similar to observations for thermal HIFU, but energy densities here are not expected to cause any significant heating. The maximum bubble radius \bar{R}_{\max} does not depend on the gel's stiffness, while the most expected bubble radius $\langle R \rangle$ has a weak dependence. These statistical observations in agar phantoms are consistent with a fatigue-based model of bubble dynamics in a viscoelastic medium (Movahed *et al.* 2016). The bubble clouds evolve to denser clouds at higher PRF and numbers of cycles and higher agar concentrations. These observations confirm that BWL, similar to SWL, causes cavitation inside tissue-mimicking phantoms and, consequently, cavitation-induced damage. The current experimental observations show a route for cavitation-induced damage spread inside soft materials. Current observations in soft tissue-mimicking phantoms with concurrent efforts on studying stone comminution by BWL pulses (Maxwell *et al.* 2015) will guide the development of effective and safe BWL technology.

Acknowledgments—The authors are grateful for fruitful discussions with T. Colonius, K. Maeda, M. R. Bailey and B. Cunitz. This work was supported by NIH NIDDK grant number P01-DK043881 and K01-DK104854.

REFERENCES

- Bailey MR, Couret LN, Sapozhnikov OA, Khokhlova VA, Ter Haar G, Vaezy S, Shi X, Martin R, Crum LA. Use of overpressure to assess the role of bubbles in focused ultrasound lesion shape *in vitro*. *Ultrasound Med Biol* 2001;27:695–708.
- Bailey MR, Pishchalnikov YA, Sapozhnikov OA, Cleveland RO, McAteer JA, Miller NA, Pishchalnikova IV, Connors BA, Crum LA, Evan AP. Cavitation detection during shock-wave lithotripsy. *Ultrasound Med Biol* 2005;31:1245–1256.
- Chavier F, Chapelon JY, Gelet A, Cathignol D. Modeling of high-intensity focused ultrasound-induced lesions in the presence of cavitation bubbles. *J Acoust Soc Am* 2000;108:432–440.
- Choi I, Shield RT. Second-order effects in problems for a class of elastic materials. *Z Angew Math Phys* 1981;32:361–381.
- Coussios CC, Roy RA. Applications of acoustics and cavitation to noninvasive therapy and drug delivery. *Annu Rev Fluid Mech* 2008;40:395–420.
- Crum LA. Nucleation and stabilization of microbubbles in liquids. *Appl Sci Res* 1982;38:101–115.
- Daniels S, Blondel D, Crum LA, ter Haar GR, Dyson M. Ultrasonically induced gas bubble production in agar based gels: Part I, experimental investigation. *Ultrasound Med Biol* 1987;13:527–539.
- Dunmire B, Kucewicz JC, Mitchell SB, Crum LA, Sekins KM. Characterizing an agar/gelatin phantom for image guided dosing and feedback control of high-intensity focused ultrasound. *Ultrasound Med Biol* 2013;39:300–311.
- Evan AP, Willis LR, Lingeman JE, McAteer JA. Renal trauma and the risk of long-term complications in shock wave lithotripsy. *Nephron* 1998;78:1–8.
- Evan AP, Willis LR, McAteer JA, Bailey MR, Connors BA, Shao Y, Lingeman JE, Williams JC, Fineberg NS, Crum LA. Kidney damage and renal functional changes are minimized by waveform control that suppresses cavitation in shock wave lithotripsy. *J Urol* 2002;168:1556–1562.
- Hall TJ, Bilgen M, Insana MF, Krouskop TA. Phantom materials for elastography. *IEEE Trans Ultrason Ferroelectr Freq Control* 1997;44:1355–1365.
- Hall TL, Kieran K, Ives K, Fowlkes JB, Cain CA, Roberts WW. Histotripsy of rabbit renal tissue *in vivo*: Temporal histologic trends. *J Endourol* 2007;21:1159–1166.
- Hamaguchi F, Ando K. Linear oscillation of gas bubbles in a viscoelastic material under ultrasound irradiation. *Phys Fluids* 2015;27:113103.
- Haralock RM, Shapiro LG. Computer and robot vision. Vol. 1. Chicago: Addison-Wesley Longman; 1992.
- Hempel CR, Hall TL, Cain CA, Fowlkes JB, Xu Z, Roberts WW. Histotripsy fractionation of prostate tissue: Local effects and systemic response in a canine model. *J Urol* 2011;185:1484–1489.
- Hyon SH, Cha WI, Ikada Y. Preparation of transparent poly (vinyl alcohol) hydrogel. *Polym Bull* 1989;22:119–122.
- Khokhlova TD, Wang Y, Simon JC, Cunitz BW, Starr F, Paun M, Crum LA, Bailey MR, Khokhlova VA. Ultrasound-guided tissue fractionation by high intensity focused ultrasound in an *in vivo* porcine liver model. *Proc Natl Acad Sci USA* 2014;111:8161–8166.
- Khokhlova VA, Bailey MR, Reed JA, Cunitz BW, Kaczkowski PJ, Crum LA. Effects of nonlinear propagation, cavitation, and boiling in lesion formation by high intensity focused ultrasound in a gel phantom. *J Acoust Soc Am* 2006;119:1834–1848.
- Kolios MC, Sherar MD, Hunt JW. Blood flow cooling and ultrasonic lesion formation. *Med Phys* 1996;23:1287–1298.
- Martins dos Santos VAP, Leenen EJTM, Rippoll MM, van der Sluis C, van Vliet T, Tramper J, Wijffels RH. Relevance of rheological properties of gel beads for their mechanical stability in bioreactors. *Biotechnol Bioeng* 1997;56:517–529.
- Maxwell AD, Cain CA, Hall TL, Fowlkes JB, Xu Z. Probability of cavitation for single ultrasound pulses applied to tissues and tissue-mimicking materials. *Ultrasound Med Biol* 2013;39:449–465.
- Maxwell AD, Cunitz BW, Kreider W, Sapozhnikov OA, Hsi RS, Harper JD, Bailey MR, Sorensen MD. Fragmentation of urinary calculi *in vitro* by burst wave lithotripsy. *J Urol* 2015;193:338–344.
- Meaney PM, Cahill MD, ter Haar GR. The intensity dependence of lesion position shift during focused ultrasound surgery. *Ultrasound Med Biol* 2000;26:441–450.
- Movahed P, Kreider W, Maxwell AD, Hutchens SB, Freund JB. Cavitation-induced damage of soft materials by focused ultrasound bursts: A fracture-based bubble dynamics model. *J Acoust Soc Am* 2016;140:1347–1386.
- Normand V, Lootens DL, Amici E, Plucknett KP, Aymard P. New insight into agarose gel mechanical properties. *Biomacromolecules* 2000;1:730–738.
- Otsu N. A threshold selection method from gray-level histograms. *Automatica* 1975;11:285–296.
- Paterson RF, Lifshitz DA, Lingeman JE, Evan AP, Connors BA, Fineberg NS, Williams JC Jr, McAteer JA. Stone fragmentation during shock wave lithotripsy is improved by slowing the shock wave rate: Studies with a new animal model. *J Urol* 2002;168:2211–2215.
- Pennes HH. Analysis of tissue and arterial blood temperatures in the resting human forearm. *J Appl Physiol* 1948;1:93–122.

- Pishchalnikov YA, McAteer JA, Williams JC Jr, Pishchalnikova IV, Vonderhaar RJ. Why stones break better at slow shockwave rates than at fast rates: *In vitro* study with a research electrohydraulic lithotripter. *J Endourol* 2006;20:537–541.
- Pishchalnikov YA, Sapozhnikov OA, Bailey MR, Williams JC Jr, Cleveland RO, Colonius T, Crum LA, Evan AP, McAteer JA. Cavitation bubble cluster activity in the breakage of kidney stones by lithotripter shockwaves. *J Endourol* 2003;17:435–446.
- Plesset MS, Prosperetti A. Bubble dynamics and cavitation. *Ann Rev Fluid Mech* 1977;9:145–185.
- Rassweiler JJ, Knoll T, Köhrmann K, McAteer JA, Lingeman JE, Cleveland RO, Bailey MR, Chaussy C. Shock wave technology and application: An update. *Eur Urol* 2011;59:784–796.
- Rayleigh JWS. On the pressure developed in a liquid during the collapse of a spherical cavity. *Phil Mag* 1917;34:94–98.
- Roberts WW, Hall TL, Ives K, Wolf JS, Fowlkes JB, Cain CA. Pulsed cavitation ultrasound: A noninvasive technology for controlled tissue ablation (histotripsy) in the rabbit kidney. *J Urol* 2006;175:734–738.
- Robinson TC, Lele PP. An analysis of lesion development in the brain and in plastics by high-intensity focused ultrasound at low-megahertz frequencies. *J Acoust Soc Am* 1972;51:1333–1351.
- Sanghvi NT, Fry FJ, Bihle R, Foster RS, Phillips MH, Syrus J, Zaitsev AV, Hennige CW. Noninvasive surgery of prostate tissue by high-intensity focused ultrasound. *IEEE Trans Ultrason Ferroelectr Freq Control* 1996;43:1099–1110.
- Sapozhnikov OA, Khokhlova VA, Bailey MR, Williams JC Jr, McAteer JA, Cleveland RO, Crum LA. Effect of overpressure and pulse repetition frequency on cavitation in shock wave lithotripsy. *J Acoust Soc Am* 2002;112:1183–1195.
- Vlaisavljevich E, Lin K, Maxwell A, Warnez MT, Mancina L, Singh R, Putnam AJ, Fowlkes B, Johnsen E, Cain C, Xu Z. Effects of ultrasound frequency and tissue stiffness on the histotripsy intrinsic threshold for cavitation. *Ultrasound Med Biol* 2015;41:1651–1667.
- Vlaisavljevich E, Maxwell A, Warnez M, Johnsen E, Cain C, Xu Z. Histotripsy-induced cavitation cloud initiation thresholds in tissues of different mechanical properties. *IEEE Trans Ultrason Ferroelectr Freq Control* 2014;61:341–352.
- Wang TY, Xu Z, Hall TL, Fowlkes JB, Cain CA. An efficient treatment strategy for histotripsy by removing cavitation memory. *Ultrasound Med Biol* 2012;38:753–766.
- Watkin NA, ter Haar GR, Rivens I. The intensity dependence of the site of maximal energy deposition in focused ultrasound surgery. *Ultrasound Med Biol* 1996;22:483–491.
- Xu Z, Ludomirsky A, Eun LY, Hall TL, Tran BC, Fowlkes JB, Cain CA. Controlled ultrasound tissue erosion. *IEEE Trans Ultrason Ferroelectr Freq Control* 2004;51:726–736.
- Yang X, Church CC. A model for the dynamics of gas bubbles in soft tissue. *J Acoust Soc Am* 2005;118:3595–3606.
- Zell K, Sperl JI, Vogel MW, Niessner R, Haisch C. Acoustical properties of selected tissue phantom materials for ultrasound imaging. *Phys Med Biol* 2007;52:N475–N484.